coatings

MDPI

Article

Corrosion Resistance of Plasma-Nitrided AISI 316L Stainless Steel with Intermittent Nitrogen Flow

Andrey Matheus Vianna [1], Oriana Palma Calabokis [2,3], Yamid E. Nuñez de la Rosa [2,3], Cláudia Eliana Bruno Marino [4], Paulo César Borges [1], Euclides Alexandre Bernardelli [1] and Márcio Mafra [1,*]

[1] Department of Mechanical Engineering, Federal University of Technology–Paraná, Campus Ecoville, Curitiba 81280-340, PR, Brazil; andreyvianna@alunos.utfpr.edu.br (A.M.V.); pborges@utfpr.edu.br (P.C.B.); ebernardelli@utfpr.edu.br (E.A.B.)
[2] Faculty of Engineering and Basic Sciences, Fundación Universitaria Los Libertadores, Bogotá 111221, Colombia; opalmac@libertadores.edu.co (O.P.C.); yenunezd@libertadores.edu.co (Y.E.N.d.l.R.)
[3] Research Center for Rheology and Non-Newtonian Fluids—CERNN, Soft Matter Research Center—SOFMAT, Federal University of Technology—Paraná–UTFPR, Rua Deputado Heitor Alencar Furtado, 5000, Bloco N, Ecoville, Curitiba 81280-340, PR, Brazil
[4] Program in Engineering and Materials Science (PIPE), Department of Mechanical Engineering, Centro Politécnico, Federal University of Paraná, Curitiba 81531-980, PR, Brazil; claudiamarino@ufpr.br
* Correspondence: mafra@utfpr.edu.br

Highlights

What are the main findings?

- Nitrogen duty cycle influenced passive film stability and corrosion resistance.
- Continuous nitrogen flow improved corrosion resistance but increased brittleness.
- 50% nitrogen duty cycle improved hardness while maintaining corrosion resistance.
- 10% nitrogen duty cycle caused a reduction in passive film stability.

What are the implications of the main findings?

- Nitrogen duty cycle offers a flexible strategy for surface engineering of nitrided layers.
- Intermittent nitrogen flow balances hardness, corrosion resistance, and crack susceptibility.

Abstract

Low-temperature plasma nitriding of austenitic stainless steels produces an expanded austenite (γ_N) layer that enhances surface hardness but may generate high residual stress and cracking, compromising corrosion resistance. This work evaluates the influence of nitrogen flow duty cycle on the corrosion resistance of AISI 316L austenitic stainless steel plasma-nitrided at 425 °C for 2 h. Continuous nitrogen flow (2C) and intermittent flow at 50% (2P50) and 10% (2P10) nitrogen duty cycles were investigated, with untreated steel (UN) as reference. Samples were characterized by SEM, XRD, nanoindentation, OCP, EIS, potentiodynamic polarization in 3.5 wt.% NaCl and XPS. Reducing the nitrogen duty cycle produced layers with lower nitrogen incorporation and reduced cracking. However, excessive reduction in the duty cycle decreased corrosion resistance, indicating the importance of sufficient nitrogen incorporation for electrochemical performance. The 2C condition exhibited the most noble corrosion potential and the highest localized corrosion potential, whereas 2P10 showed lower corrosion resistance than UN. EIS indicated more stable, thicker passive films at 2C and 2P50. The results suggest that nitrogen availability influences passive-film stability and may contribute to the synergistic protective effect of nitrogen and molybdenum. Overall, 2P50 provided a balance between surface hardening, layer integrity, and corrosion resistance.

Check for updates

Academic Editor: Yingliang Cheng

Received: 31 August 2026
Revised: 2 October 2026
Accepted: 13 October 2026
Published: 16 October 2026

Copyright: © 2026 by the authors. Licensee MDPI, Basel, Switzerland. This article is an open access article distributed under the terms and conditions of the Creative Commons Attribution (CC BY) license.

Keywords: AISI 316L; stainless steel; corrosion; plasma nitriding; intermittent nitrogen flow

1. Introduction

Stainless steels play a fundamental role in industry, including the medical field [1–3] and aggressive environments involving high temperatures, such as oil and gas extraction [4–6]. Among these steels, austenitic stainless steels are widely recognized for their excellent corrosion resistance. However, in many applications, wear resistance and surface hardness are also required, which limits their use without appropriate surface treatments [3,6–10].

Low-temperature plasma nitriding has been widely employed to overcome these limitations [1,3,10–12]. The corrosion behavior of the nitrided steel depends fundamentally on the characteristics of the resulting surface layer. Several studies have reported significant improvements in electrochemical performance when expanded austenite is formed without nitride precipitation [8,13,14]. Conversely, reductions in corrosion resistance of nitrided stainless steels have been associated with chromium nitride precipitation [1,15], crack formation [16], or insufficient nitrogen incorporation to promote the expected beneficial effects [17]. These findings indicate that corrosion resistance is governed by the balance between the beneficial effects of nitrogen enrichment and the detrimental effects of microstructural changes that may be induced by the nitriding process.

Several strategies have been proposed to minimize nitride precipitation and the brittleness of the nitrided layer, including reducing the treatment temperature [18–21] and duration [22], as well as modifying the gas mixture [23]. However, these approaches generally reduce the nitriding kinetics, which may impair layer growth and limit the development of the desired surface properties.

Another approach, investigated by Fernandes et al. (2017) [24], involves a post-nitriding treatment referred to as "denitriding", which aims to reduce residual stresses and mitigate the brittle behavior of the nitrided layer. Following the denitriding process, the authors observed a reduction in both the nitrogen concentration and the hardness of the nitrided layer. However, because this treatment is applied after nitriding, it does not eliminate chromium nitrides or heal cracks that have already formed during the nitriding process or as a consequence of it.

The strategy of using intermittent nitrogen flow to control nitrogen incorporation during plasma nitriding was first investigated by Vianna et al. (2020) [25] and dos Reis et al. (2020) [26], at treatment temperatures of 425 °C and 450 °C, respectively. Their results showed that reducing the nitrogen duty cycle decreased the nitrogen concentration in the nitrided layer, lowering chromium nitride precipitation and mitigating surface cracking. Subsequently, Sphair et al. (2025) [27] provided further insight into this process through experiments conducted at 400 °C using optical emission spectroscopy. Their results demonstrated that interrupting the nitrogen supply leads to alternating periods of surface nitrogen enrichment and nitrogen diffusion towards the bulk. Based on these findings, the authors proposed that, during nitrogen flow interruption, the supersaturation near the surface is reduced, thereby promoting nitrogen redistribution during treatment. Furthermore, nitrogen duty cycles of 25% and 50% yielded layer thicknesses and hardness values comparable to those obtained under continuous nitriding, highlighting the potential of this approach to control nitrogen incorporation without significantly compromising the nitrided layer's properties.

Although these studies have demonstrated the potential of intermittent nitrogen flow to control nitrogen incorporation and tailor the characteristics of the nitrided layer, most investigations have focused on microstructural evolution, phase formation, and

mechanical properties, particularly hardness. In contrast, its implications for corrosion resistance have not yet been investigated, especially regarding electrochemical behavior and passive film stability. Considering that corrosion resistance is closely related to the characteristics of the nitrided layer, including its composition, defect density, and passive film stability, a comprehensive electrochemical assessment is essential to understand the effects of intermittent nitrogen flow. Thus, a gap remains in understanding the relationship between the microstructural and mechanical modifications promoted by the treatment and the resulting electrochemical behavior.

To address this gap, the present work evaluates the influence of intermittent nitrogen flow on the corrosion resistance of low-temperature plasma-nitrided AISI 316L austenitic stainless steel. To clarify these relationships, the characteristics of the nitrided layer, the composition and stability of the passive film, and the electrochemical behavior of the material were investigated using complementary characterization techniques.

2. Materials and Methods

The material studied was AISI 316L austenitic stainless steel (supplied by Villares Metals S.A., São Paulo, Brazil), initially in the form of a drawn bar with a diameter of 15.8 mm (5/8 in.). To relieve residual stress and homogenize the chemical composition, the material was solution heat-treated in a salt bath at 1100 °C for 18 min, followed by water quenching. Samples were cut to a thickness of 6 mm, all faces were ground to a grit size of 1200, and then the flat faces were polished with 1 μm alumina. The chemical composition of the samples is presented in Table 1.

Table 1. Chemical composition of AISI 316L austenitic stainless steel (wt.%).

Cr	Ni	Mo	Mn	C	S	Si	Fe
17.1	10.6	1.67	1.66	0.012	0.018	0.28	Bal.

The nitriding treatments were performed in an in-house-built cold-wall reactor at the university, previously described in [27], using a pulsed direct current power supply. To evaluate the influence of intermittent nitrogen flow on plasma nitriding, samples were treated at nitrogen duty cycles of 50% (2P50) and 10% (2P10), where the duty cycle represents the ratio of the time during which the nitrogen flow remained active to the total treatment duration. Nitrogen was intermittently supplied during nitriding in 20-min cycles, repeated until the end of the treatment. Thus, for condition 2P10, at each 20-min cycle at the nitriding temperature, nitrogen flows for 2 min and is interrupted for 18 min. In addition to the intermittent nitrogen-flow conditions, untreated samples (UN) and samples nitrided under continuous nitrogen flow (2C) were analyzed as reference conditions.

In each treatment cycle, before reaching the nitriding temperature, a sputter-cleaning step was performed in an argon–hydrogen atmosphere at 300 °C for 20 min. The parameters used in the nitriding treatments are presented in Table 2.

After nitriding, the samples were characterized by scanning electron microscopy (SEM, Zeiss, model EVO MA 15, Carl Zeiss Ltd., Cambridge, UK) to measure layer thickness, X-ray diffraction (XRD, Shimadzu, model XRD-7000, Shimadzu Corporation, Tokyo, Japan) to identify phases, nanoindentation to determine surface hardness, and electrochemical tests to evaluate corrosion resistance.

For SEM analysis, one sample from each nitrided condition was cross-sectioned, mounted in bakelite, and prepared using standard metallographic procedures. Chemical etching to reveal the microstructure and the nitrided layer was performed with Marble's reagent (1 g $CuSO_2$, 5 mL HCl, 5 mL H_2O) for 50 s. XRD analysis was performed using

a diffractometer (GIXRD: Shimadzu, model XRD-7000, Shimadzu Corporation, Tokyo, Japan) with the following parameters: grazing incidence angle of 3°, Cu-Kα radiation (λ = 1.54060 Å), 30 kV, and 30 mA. Diffractogram analysis was performed using the integrated software (version 7.00) and the ICDD PDF-2 (release 2012) database.

Table 2. Nitriding parameters.

Parameters	Sputtering	Nitriding
Duration	20 min	2 h
Temperature	300 ± 3 °C	425 ± 3 °C
Pressure	3 Torr	4 Torr
Voltage	500 V	500 V
T_{on} *	35–40 µs	45–70 µs
T_{off}	200 µs	200 µs
Gas Mixture	50% H_2 + 50% Ar Total flow: 200 cm^3/min	With N_2 flow: 25% N_2 + 25% H_2 + 50% Ar Total flow: 200 cm^3/min Without N2 flow: 33.3% H_2 + 66.7% Ar Total flow: 150 cm^3/min

* T_{on} adjust was used to control treatment temperature.

The X-ray beam interaction depth was calculated using Equation (1) [28]:

$$x = \frac{-1}{\mu} \times \left[\frac{ln(1 - G_x\}}{\frac{1}{sin(\alpha)} + \frac{1}{sin(\beta)}} \right] \quad (1)$$

where μ is the linear absorption coefficient, G_x is the diffracted intensity fraction, and α and β are the incidence and diffraction angles, respectively. Because the diffraction intensity decreases exponentially with depth due to absorption, an effective interaction depth must be defined by selecting a fraction of the total diffracted intensity. In this work, a value of G_x = 95% was adopted, as also used by Sphair et al. (2025) [27], meaning that the calculated depth corresponds to the region from which approximately 95% of the diffracted intensity originates. Although a criterion based on a higher fraction, such as 99%, could also be applied, this would result in an estimated depth approximately 54% greater while accounting for only 4 additional percentage points of diffracted intensity. For the calculations, an absorption coefficient of 1816 cm^{-1} was used [23]. Under these conditions, the estimated X-ray interaction depth was 0.8 µm for a 3° incidence angle.

The nitrogen concentration at the surface was estimated for the (111) and (200) planes from the shift in the peaks of the expanded austenite relative to the original peak, following the method proposed by Öztürk and Williamson [29]. To calculate this shift, the following equations were used.

$$a_{\gamma_N} = a_\gamma + \alpha C_N \quad (2)$$

$$d_{hkl} = \frac{a}{\sqrt{h^2 + k^2 + l^2}} \quad (3)$$

where a_γ is the austenite lattice parameter (Å), a_{γ_N} is the expanded austenite lattice parameter (Å), α is the Vegard constant (0.078 Å/at%N) [25], d_{hkl} is the interplanar spacing, and h, k, and l are the Miller indices of the crystallographic planes.

Hardness was obtained by the quasi-continuous stiffness measurement (QCSM) method using a ZHN Zwick Roell instrument (GmbH & Co. KG, Ulm, Germany), where 30 indentations were performed with a maximum load of 500 mN.

The corrosion resistance of the samples was evaluated using open-circuit potential (OCP), electrochemical impedance spectroscopy (EIS), and potentiodynamic polarization (PP). Samples were immersed in 200 mL of 3.5 wt.% NaCl solution at room temperature (20 ± 2 °C) and kept immersed for 24 h before testing. After the 24 h immersion period, samples underwent 1 h of OCP monitoring to assess potential stability before EIS and PP measurements. A three-electrode system connected to a potentiostat Gamry Reference 620 (Gamry Instruments, Inc., Warminster, PA, USA) was used: a saturated calomel electrode (SCE) as the reference electrode, a graphite counter electrode, and the sample itself as the working electrode. Three samples from each condition were prepared as working electrodes and embedded in epoxy resin to expose a single face measuring 1.96 cm^2. Specifically for the UN condition, the exposed face was ground to 400 grit to equalize the surface roughness parameter Ra with that of the nitrided samples. EIS and PP tests were performed using a Gamry Reference 620 potentiostat. EIS was conducted over a frequency range of 10^{-2} to 10^6 Hz, with 5 points per decade and VRMS = 0.01 V. PP was performed at a scan rate of 1 mV/s, from –0.2 V vs. OCP to +1.2 V vs. OCP. All potentials reported in this work are referenced to the saturated calomel electrode (SCE). Sample surfaces were examined by SEM after potentiodynamic polarization tests to analyze localized corrosion.

Polarization resistance (R_P) values were graphically estimated from Nyquist diagrams by extrapolating the capacitive arc to the real axis using a second-order polynomial fit. At high frequencies, impedance is dominated by the solution resistance (R_S), while at low frequencies the response is primarily influenced by R_P, obtained as the difference between total resistance (R_T) and R_S, as shown in Equation (4) [30]:

$$R_P = R_T - R_S \tag{4}$$

The passive layer capacitance (C_P) was calculated from the capacitive region of the Bode diagram, in which the system exhibits predominantly capacitive behavior (phase angle close to $-90°$). In this region, the log | Z | vs. log f curve displays a characteristic slope of -1, allowing the capacitance to be calculated using Equation (5) [30]:

$$C_P = \frac{1}{2\pi f|Z|} \tag{5}$$

For simplification, the value of C_P was calculated considering a frequency of $1/2\pi$ Hz, allowing the use of the form shown in Equation (6):

$$C_P = \frac{1}{|Z|_{f=1/2\pi\ \mathrm{Hz}}} \tag{6}$$

Finally, X-ray photoelectron spectroscopy (XPS) was employed to identify the elemental chemical states in the corrosion products qualitatively and to compare the chemical species formed under different treatment conditions. Measurements were performed at UDESC–Joinville using a Thermo Scientific K-Alpha instrument with an Al-Kα ionization source (hν = 1486.6 eV). High-resolution spectra were collected for Fe (2p), Cr (2p), and O (1s) with a pass energy of 200 eV and an energy step of 0.025 eV.

3. Results and Discussion

3.1. Layer Thickness

SEM cross-sectional micrographs of the nitrided layers for conditions 2C, 2P50, and 2P10 are presented in Figure 1.

In all analyzed conditions, double layers were observed, consisting of an outer nitrogen-rich layer (γ_N) and an inner carbon-rich layer (γ_C). The formation of the γ_C

layer stems from the accumulation of carbon at the end of the γ_N layer [14]. Nevertheless, the carbon concentration in the γ_C layer is insufficient to achieve the same hardening effect as nitrogen in the γ_N layer, resulting in lower hardness values [23].

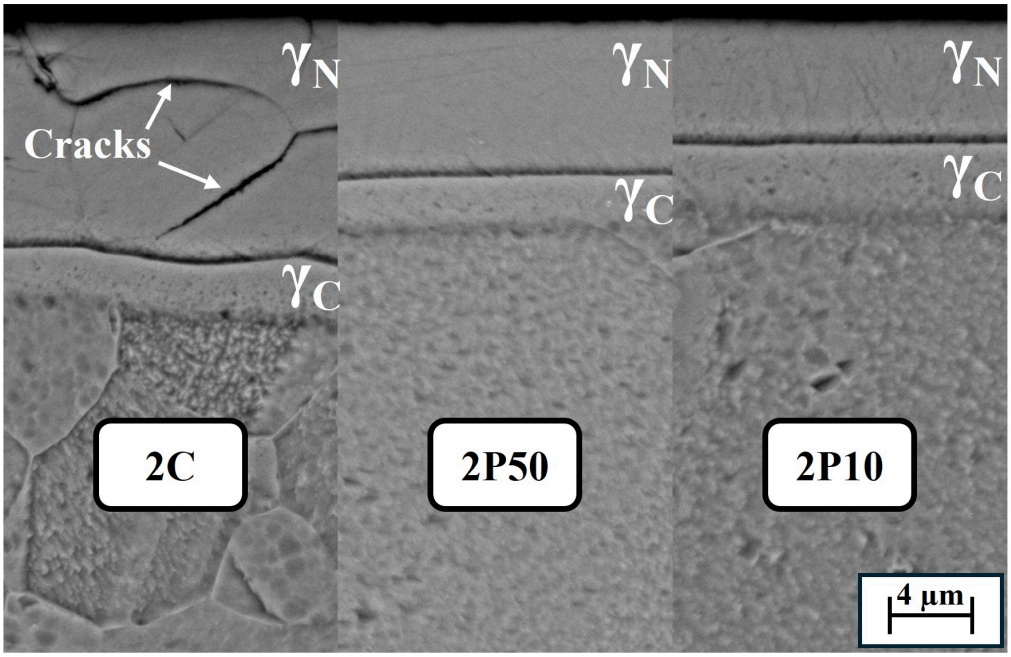


Figure 1. Scanning electron microscopy (SEM) micrographs of the cross-sectional view of nitrided samples 2C, 2P50, and 2P10.

The migration of carbon toward the inner region of the nitrided layer is attributed to nitrogen incorporation at the material surface. Due to its higher affinity for Fe and Cr, nitrogen preferentially occupies interstitial sites, thereby displacing carbon toward deeper regions [31]. Furthermore, sputtering induced by the Ar–H_2 gas mixture can dissociate carbon atoms on the reactor walls, allowing them to diffuse into the material's bulk [32].

The thicknesses of the outer, inner, and total layers for all nitrided samples are presented in Table 3.

Table 3. Thickness of the outer layer (γ_N), inner layer (γ_C), and total layer (γ_N + γ_C) for nitrided samples 2C, 2P50, and 2P10.

Condition	Outer Layer Thickness (γ_N) (µm)	Inner Layer Thickness (γ_C) (µm)	Total Thickness (γ_N + γ_C) (µm)
2C	11.0 ± 0.9	2.5 ± 0.3	13.5 ± 1.1
2P50	7.5 ± 0.3	2.5 ± 0.1	10.0 ± 0.7
2P10	5.5 ± 0.2	3.3 ± 0.2	8.8 ± 0.7

Both the total layer thickness and the γ_N layer thickness decreased as the nitrogen duty cycle decreased. This behavior stems from lower nitrogen availability, which restricts the mechanisms of austenite expansion, including the stress gradient and nitrogen concentration in the layer [25–27].

When analyzing the γ_C layer thicknesses, condition 2P10 showed the thickest layer. This behavior is attributed to intermittent nitrogen supply and to prolonged periods without nitrogen introduced into the treatment atmosphere. According to Manova and Mändl [33], approximately 10 min of nitriding are required before austenite expansion begins. Consequently, because the nitrogen pulses in condition 2P10 lasted only 2 min per 20-min treatment, multiple cycles were required before a nitrogen-saturated layer formed,

thereby preventing further carbon diffusion. In condition 2P50, on the other hand, the 10-min pulses were sufficiently long to form a stable γ_N layer, blocking carbon diffusion and resulting in a γ_C thickness similar to that observed in condition 2C.

Figure 1 also reveals cracks in the nitrided layer in condition 2C, whereas the layers in the conditions nitrided with intermittent flow appear intact. It should be noted that the images are cross-sectional views; therefore, the observed cracks may result from cutting and metallographic preparation, since no cracks were observed on the top surface of the samples, as shown in Figure 2. Nevertheless, the absence of cracks in conditions 2P50 and 2P10 indicates reduced brittleness in the layer nitrided with intermittent nitrogen flow.

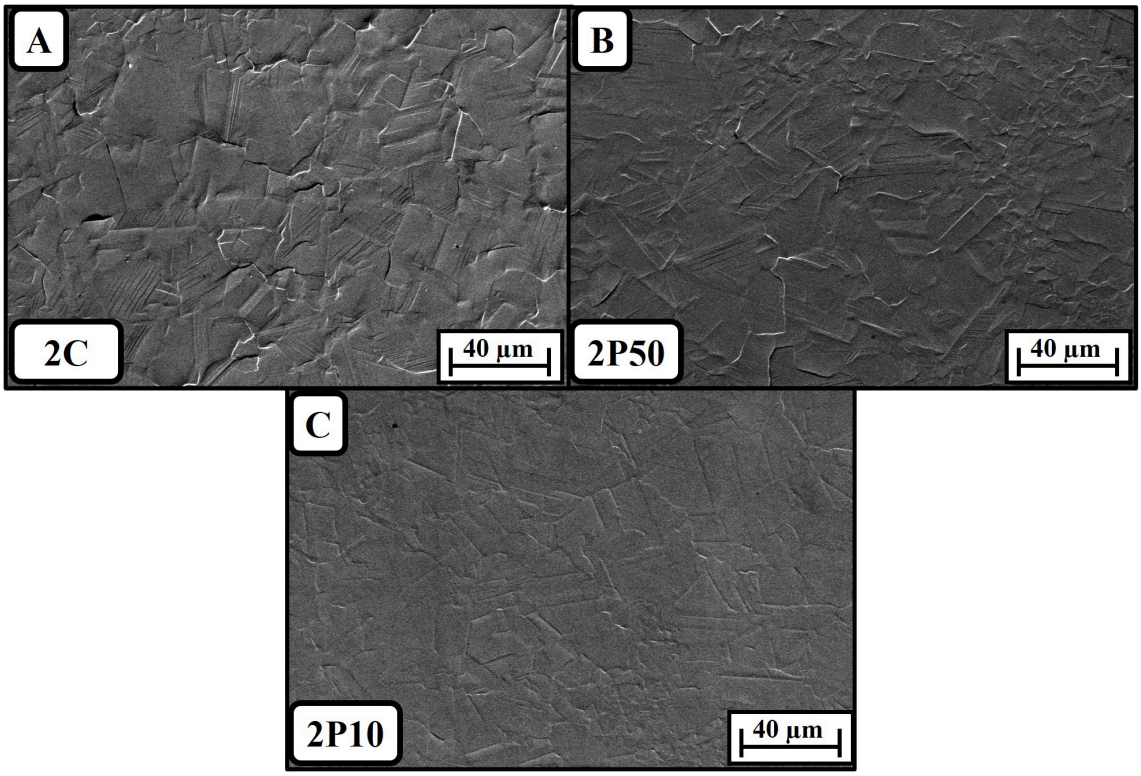


Figure 2. Scanning electron microscopy (SEM) micrographs of the top surfaces of the nitrided samples (**A**) 2C, (**B**) 2P50, and (**C**) 2P10.

3.2. X-Ray Diffraction

Figure 3 presents the X-ray diffraction results over the 2θ range of 30° to 100° in Figure 3A and 30° to 55° in Figure 3B, where the highest-intensity austenite peaks are located. A shift in the austenite peaks toward lower angles is observed, accompanied by peak broadening, which is directly associated with crystal lattice expansion and residual stresses [34,35]. The reduction in intensity, and even the disappearance of peaks at high diffraction angles, is attributed to changes in grain orientation induced during the nitriding process [36].

Analysis of Figure 3B allows a clearer visualization of the differences between the austenite peak shifts. Lower nitrogen duty cycles result in smaller lattice expansion, reflecting lower nitrogen incorporation. In samples 2C and 2P50, the presence of peaks adjacent to the main expanded austenite peaks indicates the formation of iron nitrides, as a consequence of expanded austenite decomposition [23,35]. Phase identification by XRD, supported by PDF card 00-006-0627 and the literature [18,22], indicates that the observed iron nitride phase corresponds to Fe_4N, as the diffraction peaks at approximately 41.2° and 47.9° align with its (111) and (200) crystallographic planes. No iron nitride

peaks were observed in sample 2P10, suggesting that a lower amount of nitrogen was incorporated under this condition. In general, the short treatment durations help control nitride formation [37,38], which explains the absence of chromium nitride peaks under the studied conditions.

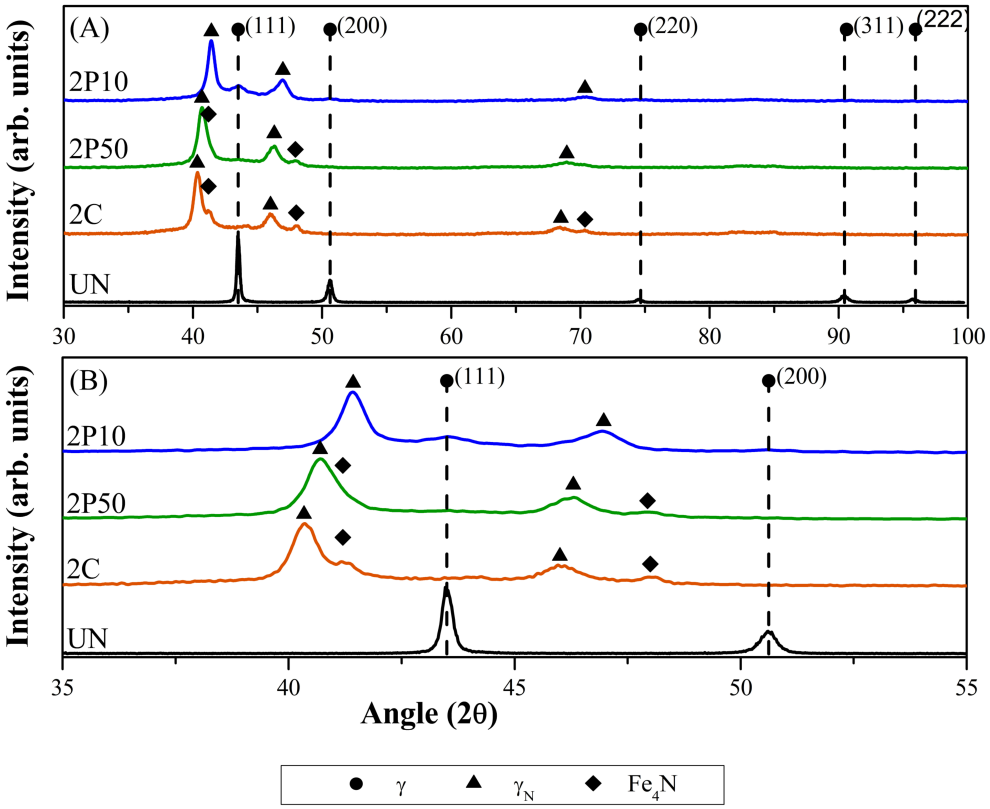


Figure 3. X-ray diffractograms of nitrided samples (2C, 2P50, and 2P10) and the untreated sample (UN) over a 2θ range of 30° to 100° in (**A**) and 30° to 55° in (**B**).

Table 4 presents the estimated nitrogen concentration values (N_C) for the (111) and (200) planes at the surface of each nitrided condition. Data from the UN condition is shown as a reference.

Table 4. Estimated nitrogen concentration (N_C) at the surface for the (111) and (200) planes obtained by X-ray diffraction for nitrided samples (2C, 2P50, and 2P10). The untreated condition (UN) serves as the reference for the austenite phase.

Condition	Plane (111)				Plane (200)				Mean N_C (at.%N)
	2θ (°)	d (Å)	a (Å)	N_C (at.%N)	2θ (°)	d (Å)	a (Å)	N_C (at.%N)	
UN	43.50	2.08	3.60	-	50.62	1.80	3.60	-	-
2C	40.34	2.23	3.87	34	46.00	1.97	3.94	43	39
2P50	40.70	2.22	3.84	30	46.30	1.96	3.92	40	35
2P10	41.43	2.18	3.77	22	46.97	1.93	3.87	34	28

The difference observed between the (111) and (200) planes is related to the anisotropy of austenite, since the Poisson ratio depends on crystallographic orientation and thereby affects nitrogen diffusivity [39].

The nitrogen concentration was highest in condition 2C for both analyzed planes, with a mean value of 39 at.%, which is reported in the literature as corresponding to a saturated nitrogen concentration [40]. Decreasing the nitrogen duty cycle resulted in lower

nitrogen concentrations, reaching mean values of 35 at.% for condition 2P50 and 28 at.% for condition 2P10, both below saturation.

On the (111) plane of condition 2P10, the surface nitrogen concentration was 22 at.%, a value close to the 15 at.%, proposed by Christiansen, Dahl and Somers [40] as corresponding to the concentration of nitrogen strongly bound to the matrix chromium. This behavior is associated with the chromium trap model, in which nitrogen exhibits low mobility due to strong interatomic interactions. Therefore, the nitrogen in the 2P10 layer is expected to exhibit limited mobility within the crystal structure. The differences in concentration between the conditions are explained not only by the lower nitrogen supply during nitriding, but also by the predominance of sputtering during nitrogen flow-off periods. This process, conducted in an Ar–H_2 atmosphere, can promote a denitriding effect, removing nitrogen from the outermost surface layers [40].

Another important aspect concerns the lattice expansion of the expanded austenite, reaching 7.5% on the (111) plane and 9.5% on the (200) plane for condition 2C, indicating a high level of residual stress. In contrast, lower expansion levels were recorded under intermittent flow; for instance, condition 2P10 exhibited values of 4.8% on the (111) plane and 7.4% on the (200) plane. This expansion is directly linked to the generation of residual stresses and non-uniform plastic deformations, which are consequences of austenite's anisotropy. Due to the low stacking-fault energy characteristic of austenitic stainless steels, these stresses also manifest on the surface as grain boundary steps and slip bands [41].

3.3. Nanohardness

The indentations performed during the hardness test are shown in Figure 4. Hardness measurement in thin hard layers on a softer substrate presents particular challenges, since the contact depth strongly influences the results. For this reason, it is recommended that the measurement depth be less than 10% of the layer thickness [42]. In addition, the heterogeneity of the nitrided layer also interferes, as different depths exhibit varying degrees of expansion, which influences the obtained values [33].

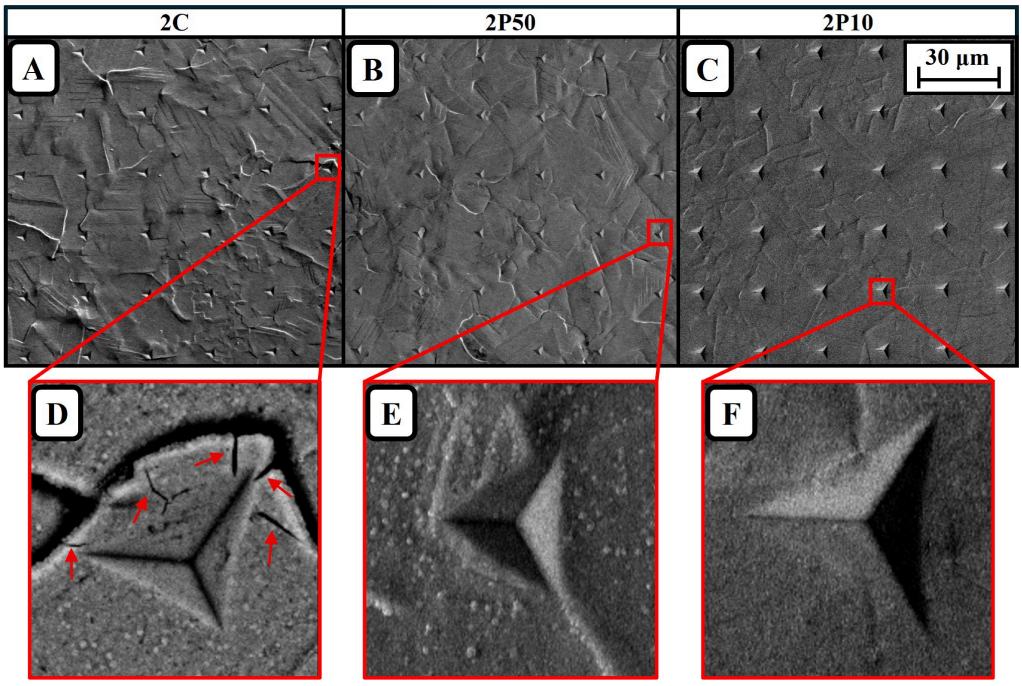


Figure 4. Scanning electron microscopy (SEM) images of the indentation arrays (**A**–**C**) and magnified views of for microcrack observation (**D**–**F**) for conditions 2C (**A**,**D**), 2P50 (**B**,**E**), and 2P10 (**C**,**F**).

Nitrogen in solid solution contributes to the hardening of the austenitic matrix by hindering dislocation motion, with higher nitrogen concentrations generally resulting in greater hardness [6]. However, the dislocation-blocking mechanism can also lead to crack formation when the applied stress exceeds the layer's fracture strength. The low ductility of the γ_N layer leads to stress relief via cracking, which introduces errors in hardness measurements, resulting in an underestimation of the layer hardness [2,40].

This condition was observed in sample 2C, which exhibited microcracks around some indentations, whereas the intermittent-flow conditions (2P50 and 2P10) remained crack-free, indicating lower brittleness. The appearance of these indentations is an initial indicator of mechanical behavior under contact loads, where a brittle surface may lead to inadequate performance. It becomes even more relevant when considering the use of stainless steels, where crack formation can expose internal regions of the material to corrosive fluids, thereby accelerating localized corrosion.

The hardness measurement results of the nitrided samples as a function of penetration depth are shown in Figure 5. The graph shows the depths reached under progressively increasing loads up to 500 mN for each sample. All conditions exhibited maximum hardness values between 3.5 and 4 times those obtained for the UN condition, reaching 12.9 GPa, 12.0 GPa, and 11.6 GPa for the 2C, 2P50, and 2P10 conditions, respectively. Decreasing the duty cycle resulted in layers with lower surface hardness; however, even the 2P10 condition exhibited a considerable increase in maximum hardness compared with the UN condition.

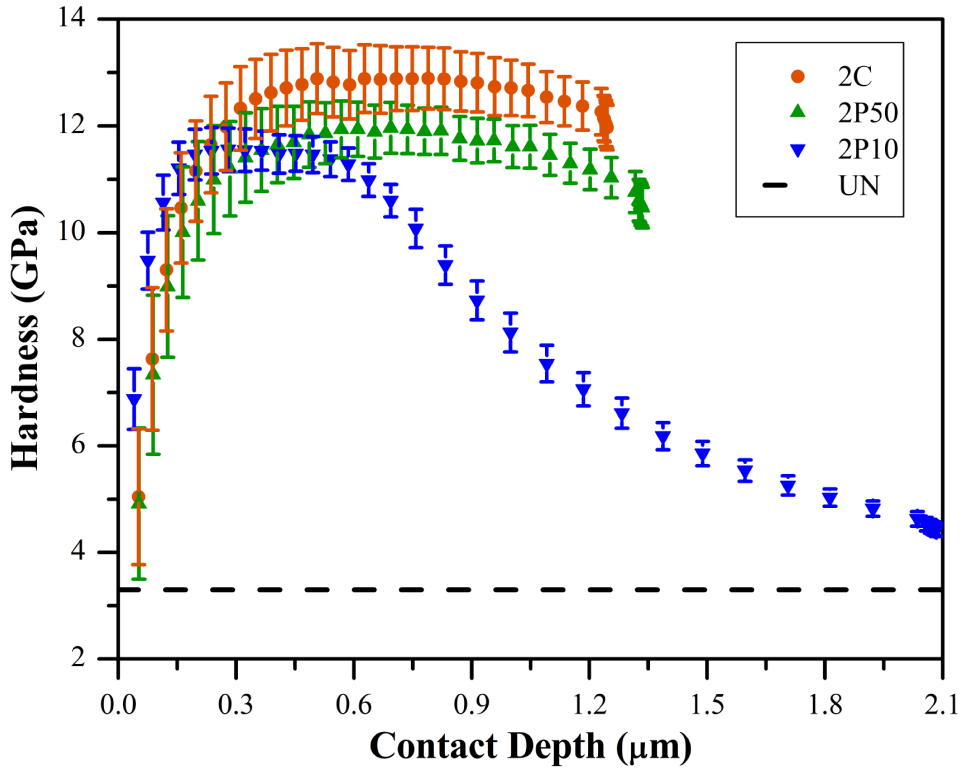


Figure 5. Hardness profile of the nitrided layer as a function of penetration depth.

Measured hardness decreases with indentation depth, a trend that is amplified at greater penetrations by the progressive contribution of the bulk substrate. The 2P10 condition exhibited the most pronounced reduction relative to the maximum hardness. This behavior may be related to the lower nitrogen concentration and the reduced thickness of the γ_N layer under these conditions. In addition, the greater thickness of the γ_C layer observed for 2P10 may contribute to the more pronounced decrease in hardness with depth, since the influence of this region is reached at shallower penetration depths. Thus, the

hardness response of the 2P10 condition is more sensitive to the transition between the nitrogen-enriched surface region and the underlying regions of the treated layer.

3.4. Electrochemical Corrosion

Open circuit potential (OCP) measurements are shown in Figure 6 and were conducted in 3.5 wt.% NaCl aqueous solution to characterize the electrochemical stability of the treated and untreated surfaces after 24 h of immersion.

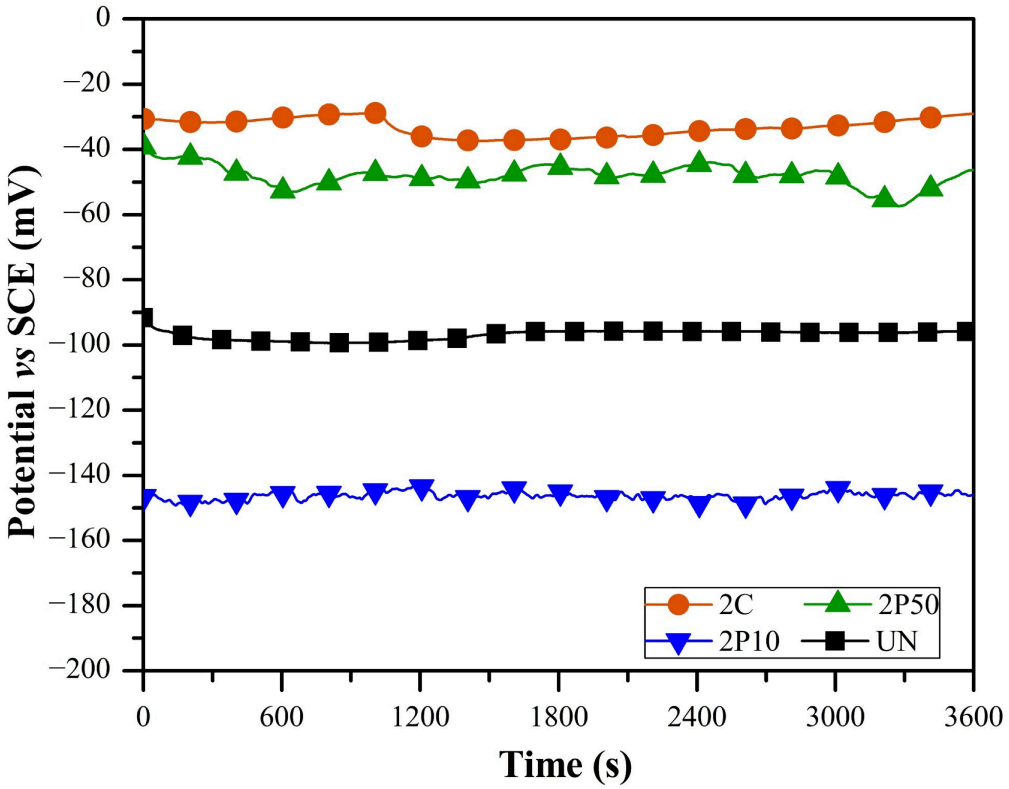


Figure 6. Evolution of open-circuit potential (OCP) as a function of time for nitrided samples (2C, 2P50, and 2P10) and an untreated sample (UN), after 24 h of pre-immersion in 3.5 wt.% NaCl aqueous solution.

It is observed that the nitrided conditions with greater nitrogen exposure time—i.e., 2C and 2P50—exhibited nobler corrosion potentials (E_{corr}), with values of –30 mV and –46 mV, respectively. These results indicate greater electrochemical stability, attributed to the formation of a more stable passive chromium oxide film due to the higher nitrogen concentration in the nitrided layer. This behavior is consistent with the findings discussed by Borgioli, Galvanetto and Bacci [13] and Luiz et al. [43].

In contrast, the sample nitrided under condition 2P10 exhibited a less noble potential (–145 mV), lower than that of the untreated sample (UN), which was –95 mV. This behavior suggests that for lower nitrogen duty cycles, the stability of the formed passive film is reduced. Such behavior can be attributed to the combination of the near-surface denitriding and the lower nitrogen concentration incorporated in this cycle, which is insufficient to overcome the detrimental effects of increased residual stresses and dislocation density induced by nitriding.

The introduction of nitrogen into austenitic stainless steel promotes the formation and maintenance of the passive chromium oxide film (Cr_2O_3). This process occurs especially through synergistic action with molybdate species, which facilitate the dissociation of

chromium hydroxides ($Cr(OH)_3$), which exhibit lower stability compared to Cr_2O_3 [43]. Thus, the protection mechanism proceeds as described in reactions (7), (8) and (9):

$$Cr(OH)_{3_{(s)}} \rightarrow CrOOH_{(s)} + O^{2-}_{(aq)} + 2H^{+}_{(aq)} \quad (7)$$

$$[N]_{(s)} + 4H^{+}_{(aq)} + 3e^{-} \rightarrow NH^{+}_{4_{(aq)}} \quad (8)$$

$$2Cr_{(s)} + 3O^{2-}_{(aq)} \rightarrow Cr_2O_{3(s)} \quad (9)$$

The beneficial effect of nitrogen on corrosion resistance primarily stems from its ability to stabilize the passive film. Nitrogen mitigates localized acidification and promotes the formation of a more protective chromium oxide layer (Cr_2O_3), particularly through its synergistic interaction with molybdenum species. The activation of this protective mechanism relies on both a sufficiently high nitrogen concentration in the nitrided layer and adequate nitrogen mobility within the crystal lattice.

Condition 2P10 exhibited a mean nitrogen concentration of 28 at.%, reaching 22 at.% in grains with (111) orientation. Since approximately 15 at.% of nitrogen is strongly bound to chromium [40], reducing its mobility, the effective amount of nitrogen available for reaction (8) is limited.

On the other hand, although condition UN does not benefit from the mechanisms described above, it also lacks features such as stress gradients and high dislocation density. Consequently, it forms a more homogeneous passive film with fewer preferential sites for corrosion initiation.

It is worth noting that the curves for conditions nitrided with intermittent nitrogen flow exhibited instability in the open-circuit potential, characterized by slight variations over time. Considering that passivation in austenitic stainless steels corresponds to a state of dynamic equilibrium, in which there is continuous competition between anodic dissolution of the film and its repassivation, the observed oscillations suggest the occurrence of local ruptures followed by subsequent recomposition.

The investigation of corrosion mechanisms and the properties of passive layers was conducted using electrochemical impedance spectroscopy (EIS). Figure 7A–C shows the Nyquist, Bode-phase, and Bode-$|Z|$ diagrams for the nitrided and untreated conditions, obtained in 3.5% NaCl solution after 24 h of pre-immersion and 1 h of OCP stabilization.

In the Nyquist diagram (Figure 7A), condition 2C exhibited the largest arc diameter, followed by condition 2P50, which displayed similar behavior. In contrast, conditions UN and 2P10 showed significantly smaller arcs. In the Bode curves (Figure 7B,C), conditions 2C and 2P50 also demonstrated similar behavior, with high phase angles ($\approx -70^{\circ}$) over a wide frequency range (10^3 to 10^{-2} Hz) and an impedance modulus exceeding 10^5 $\Omega \cdot cm^2$. Condition 2P10 showed a phase angle near -60° over a narrower frequency range (10^3 to 10^{-1} Hz), dropping to -45° at lower frequencies. This result suggests a combination of resistive and capacitive behavior due to a less-efficient passive film. It may be attributed to a combination of its high dislocation density and the lower nitrogen content of the 2P10 layer. At high frequencies (>10^4 Hz), all conditions exhibited similar impedance moduli, reflecting the electrolyte resistance.

The untreated sample (UN) exhibited a single time constant, as evidenced by a broad, highly capacitive peak (phase angle near -80°) over the frequency range of 10^3 to 10^{-2} Hz. This behavior is typically associated with the presence of a homogeneous, stable chromium oxide passive film [44].

In contrast, all nitrided samples exhibited two time constants, indicating two distinct electrochemical processes: one fast (at high frequencies) and one slow (at low frequencies). The first is associated with the interfacial response between the passive film and the

electrolyte, primarily reflecting the film capacitance and initial charge-transfer events. The second process involves charge transfer across the passive layer and/or the diffusion of ionic species in the electrolyte or within the film itself.

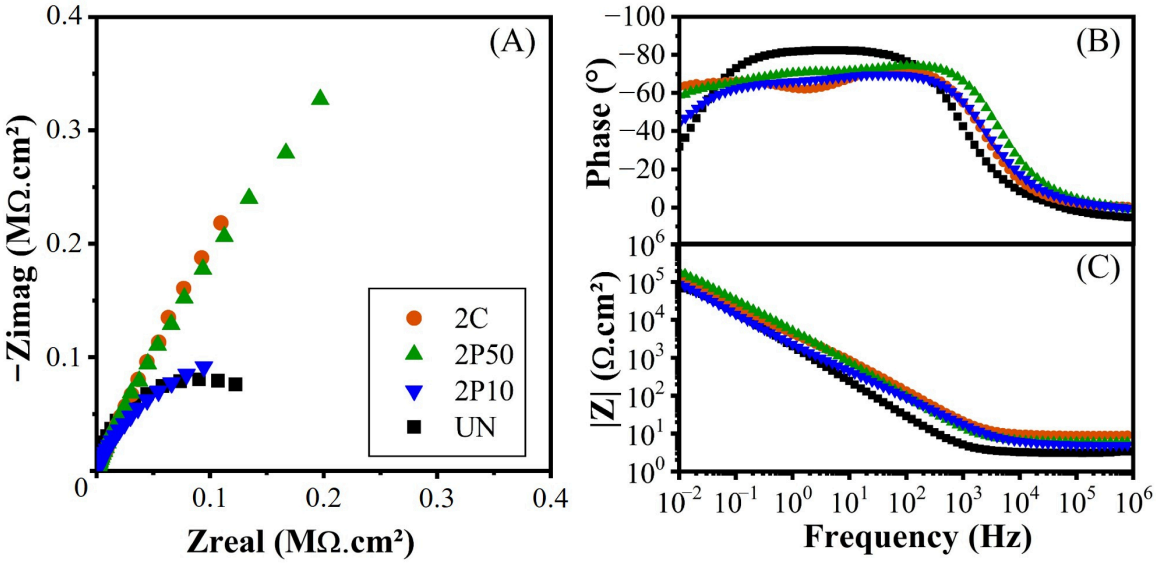


Figure 7. Electrochemical impedance diagrams for nitrided samples (2C, 2P50, and 2P10) and the untreated sample (UN), obtained in 3.5 wt.% NaCl aqueous solution at open-circuit potential (OCP) after 24 h of pre-immersion and 1 h of OCP stabilization. (**A**) Nyquist diagram; (**B**) Bode–phase angle diagram; (**C**) Bode–impedance modulus diagram.

In conditions 2P50 and 2P10, the overlap of these distinct processes is suggested by the characteristic of a prolonged plateau at high phase angles in the Bode diagrams. For condition 2C, the Bode diagram (Figure 7B) clearly shows two peaks. These findings are in agreement with the literature, which reports similar behavior in systems with modified passive films, where multiple time constants reflect the complexity of the electrochemical processes involved [14,15,43].

The polarization resistance (R_P) and passive layer capacitance (C_P) values calculated according to Equations (4)–(6) are presented in Table 5. R_P was determined graphically by extrapolating the capacitive arc in the Nyquist diagram to the real axis, and this value was corroborated by the low-frequency impedance observed in the Bode diagram.

Table 5. Polarization resistance (R_P) and passive layer capacitance (C_P) obtained for nitrided samples (2C, 2P50, and 2P10) and the untreated sample (UN) in 3.5 wt.% NaCl aqueous solution after 24 h of pre-immersion and 1 h of OCP stabilization.

Condition	R_P (MΩ·cm^2)	C_P (μF/cm^2)
2C	0.73	55.4
2P50	0.64	44.2
2P10	0.19	105.3
UN	0.16	89.7

Conditions 2C and 2P50 yielded similar results, characterized by low capacitance and high polarization resistance, indicating the formation of a stable and thicker passive film. In contrast, conditions UN and 2P10 exhibited lower R_P and higher C_P values than 2C and 2P50, indicating the formation of less protective passive films.

However, it is essential to highlight that, despite condition 2P10 presenting R_P and C_P values close to those of UN, it demonstrated inferior stability, as evidenced by less

noble corrosion potentials and higher corrosion current densities. This discrepancy is due to the high stress gradient and elevated dislocation density present in the nitrided layer of 2P10, which compromises film integrity. Conversely, the passive film of condition UN, although less robust than those of samples 2C and 2P50, offers superior protection quality compared to 2P10, owing to its greater homogeneity and the absence of structural defects and dislocations induced by the nitriding process, which would otherwise promote localized corrosion initiation.

Figure 8 shows the most representative potentiodynamic polarization curves in 3.5% NaCl solution after 24 h of pre-immersion and 1 h of OCP stabilization, while Table 6 presents the corrosion parameters and their respective standard deviations.

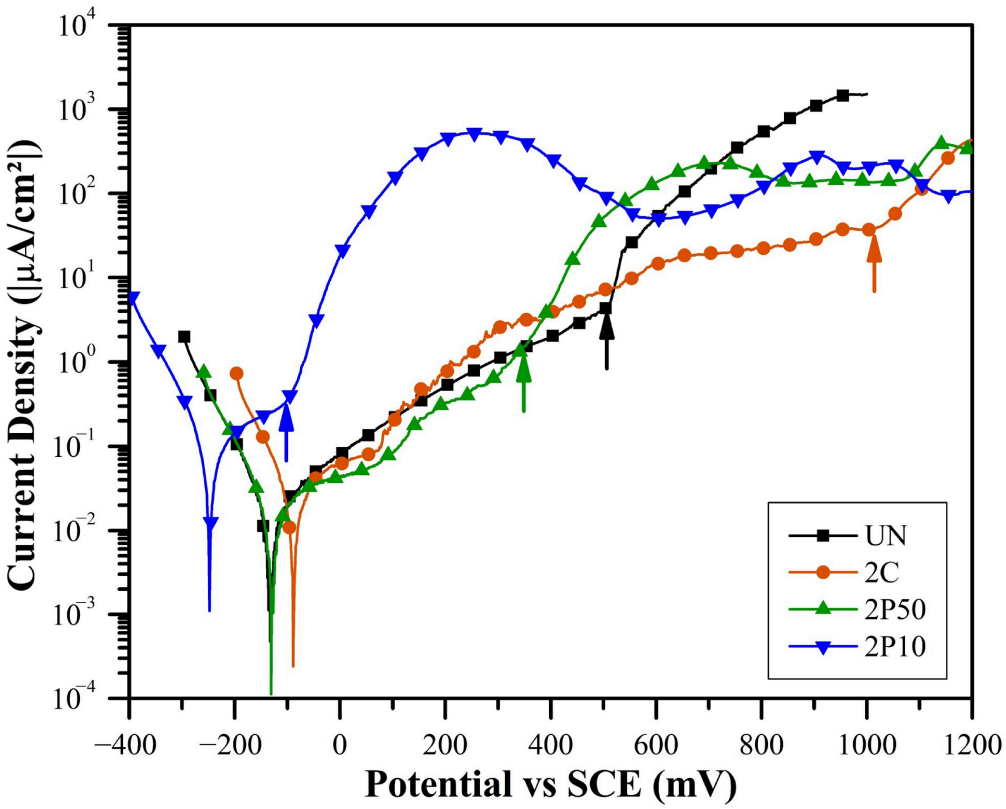


Figure 8. Potentiodynamic polarization curves for nitrided samples (2C, 2P50, and 2P10) and an untreated sample (UN), obtained after 24 h of pre-immersion and 1 h of OCP stabilization in 3.5 wt.% NaCl aqueous solution. Arrows indicate the localized corrosion potential (E_{loc}).

Table 6. Values of corrosion potential (E_{corr}), localized corrosion potential (E_{loc}), corrosion current density (I_{corr}), and localized corrosion current density (I_{loc}) obtained from the potentiodynamic polarization curves.

Condition	E_{corr} (mV)	I_{corr} ($\lvert\mu A/cm^2\rvert$)	E_{loc} (mV)	I_{loc} ($\lvert\mu A/cm^2\rvert$)
2C	-87 ± 3	0.040 ± 0.005	1033 ± 12	33.51 ± 1.27
2P50	-123 ± 9	0.025 ± 0.004	352 ± 15	2.03 ± 0.60
2P10	-256 ± 10	0.140 ± 0.037	-101 ± 5	0.32 ± 0.12
UN	-136 ± 7	0.022 ± 0.003	514 ± 20	3.50 ± 0.43

The UN condition curve exhibits the typical behavior of 316L stainless steel, with a gradual increase in current in the anodic region and an abrupt increase at the localized corrosion potential, as reported in numerous studies [1,14]. This behavior reflects the

formation of a stable passive layer, although susceptibility to localized corrosion at higher potentials is observed.

Condition 2C exhibited the best corrosion performance, evidenced by the most noble E_{corr} value (–87 mV vs. SCE) and the elevated potential required for localized corrosion (1033 mV vs. SCE). Condition 2P50, treated under a nitrogen atmosphere with a 50% duty cycle, exhibited behavior in the Tafel region similar to that of the untreated sample, with notably lower anodic current density up to approximately 350 mV. At that point, the localized corrosion process was initiated. This behavior may indicate that, although relatively stable, the passive film formed under this condition offers limited protection at elevated potentials, possibly due to lower nitrogen incorporation into solid solution than in condition 2C. Furthermore, condition 2P50 exhibited a region, between 600 mV and 1000 mV, in which the current density remained close to 100 $\mu A/cm^2$, which may be characterized as a pseudo-passivation region [45].

In condition 2P10, the more negative corrosion potential (–256 mV vs. SCE) and the initiation of localized corrosion close to E_{corr} (–101 mV vs. SCE)–corroborated by the OCP and EIS analyses–reveal the lower protective capacity of the passive film formed.

Figure 9 presents surface micrographs of the samples before and after the corrosion tests, showing localized corrosion after the potentiodynamic polarization test. In the nitrided condition, corrosion occurred predominantly at grain boundaries, whereas in the UN condition, localized corrosion was dispersed across the entire sample surface.

In condition 2C, a few larger corroded regions were observed. In sample 2P50, the number of localized corroded regions increased, while their size decreased, leading to the formation of well-defined triangular pits at grain boundaries, characteristic of crystallographic corrosion. In condition 2P10, this morphology was also observed, but with reduced symmetry and a significant increase in the number of corroded regions. This can be attributed to the formation of a less protective passive film. Thus, while in condition 2C only a few regions exhibited passive film rupture, the decrease in the films' protective performance in conditions 2P50 and 2P10 enabled rupture at more surface sites under polarization, with the particularity that the attack followed crystallographic planes under these conditions.

The formation of crystallographic pits, such as the pyramidal pits with triangular bases observed in condition 2P50 and less evidently in condition 2P10, results from the preferential electrochemical dissolution along specific crystallographic planes. It occurs because, following the rupture of the passive film at stress-induced weak points, the nitrided layer (phase γ_N) is exposed. The inherent anisotropy of the γ_N phase, with distinct stress levels and nitrogen distributions, leads to lower dissolution activation energies on specific crystallographic planes. Grain boundaries are regions of intrinsically higher energy and can accumulate residual stresses due to deformation incompatibility between adjacent grains. Consequently, they may act as preferential sites for corrosion initiation, facilitating the propagation of corrosion into the grain interior along preferential paths.

In contrast, in condition 2C, which demonstrates the best corrosion performance and the highest nitrogen concentration, failure does not manifest as a crystallographic morphology. One explanation for this behavior is the presence of microcracks, observed in Figure 1. Such microcracks may serve as initiation sites for a more extensive attack (Figure 9). It would represent more drastic ruptures of the passive layer, directing the attack in a less crystallographically selective manner, overriding the influence of subtle crystallographic weaknesses that would otherwise lead to triangular pits.

Figure 10 presents a schematic representation of the reactions at the interface between the electrolyte and the sample surfaces, highlighting an additional protective mechanism arising from the synergistic interaction between nitrogen and molybdenum under nitrided

conditions. On the left, the figure illustrates an untreated sample (UN) in contact with the electrolyte, where deprotonation of chromium hydroxide occurs, releasing O^{2-} and H^{+} ions, as shown in reaction (i). The O^{2-} ions participate in the chromium oxide-forming reaction, represented in (ii). In contrast, H^{+} ions accumulate at the interface, as highlighted in (iii), attracting chloride ions and promoting the dissolution of metallic ions at defect sites in the passive layer.

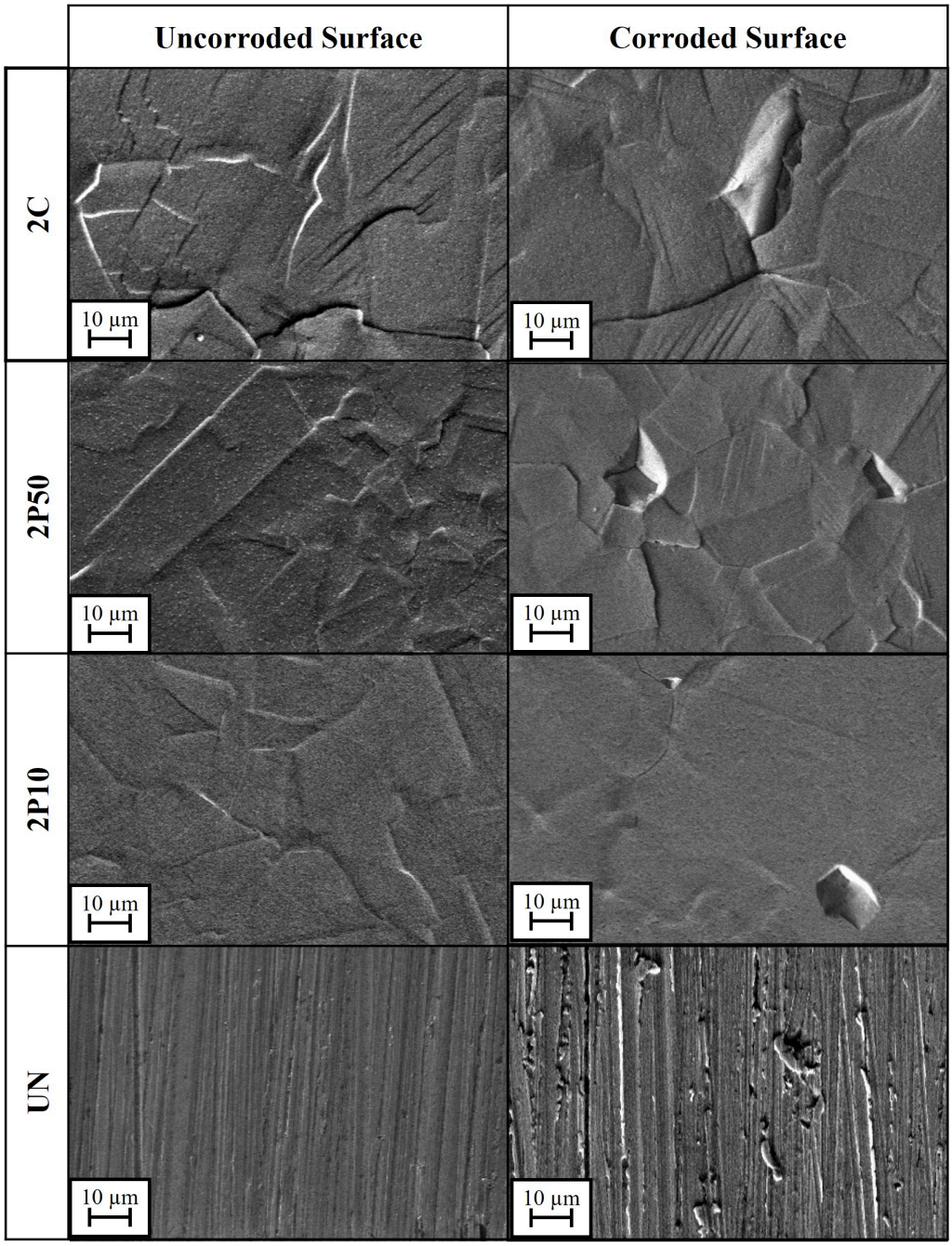


Figure 9. Scanning electron microscopy (SEM) images of nitrided samples (2C, 2P50, and 2P10) and an untreated sample (UN), before and after the potentiodynamic polarization test ((**left**) and (**right**) images, respectively), showing the presence of localized corrosion after testing.

On the right side of the figure, the nitrided surface exhibits an additional protective mechanism, as illustrated in (iv). The diffusion of nitrogen to the interface consumes H^{+} ions, forming NH_4^{+}, thereby inhibiting localized acidification, hindering chloride ion accumulation, and facilitating oxygen diffusion [43].

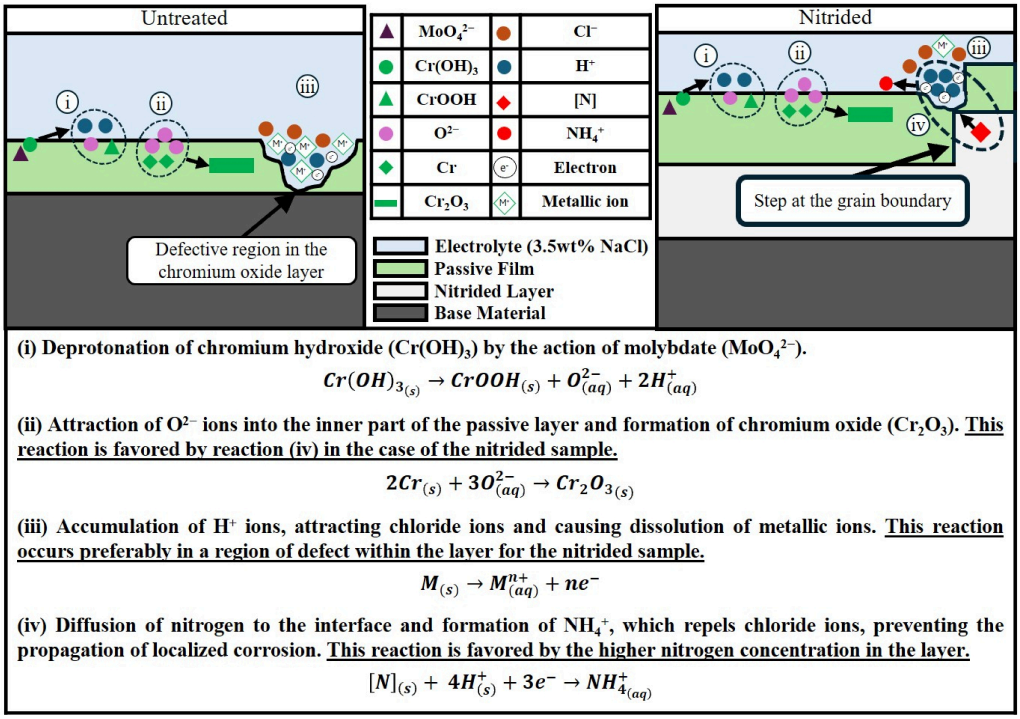


Figure 10. Schematic representation of chemical reactions at the interface between the electrolyte and the passive chromium oxide layer in untreated and nitrided samples.

This protective mechanism acts primarily at grain boundaries—regions where the presence of dislocations generated by the nitriding process hinders the formation of a uniform chromium oxide layer. It should be noted that, as the potential increases during the potentiodynamic polarization test, the reactions intensify, and the higher nitrogen concentration at the surface favors the occurrence of reaction (iv).

3.5. X-Ray Photoelectron Spectroscopy (XPS)

XPS analysis was performed on two regions of the nitrided samples subjected to potentiodynamic polarization testing: the center and the edge, to evaluate the corrosion products. For condition 2C, only a portion of the edge exhibited a color change after the polarization test, and this was the selected area. For the untreated sample (UN), which showed no change in surface color, the analysis was performed in a single region. The analyzed regions are shown in Figures 11 and 12.

The dark discoloration observed under conditions 2C and 2P50 was restricted to the edges of the samples, a region where edge effects occur during nitriding. This effect occurs at the edge due to the distortion of the charge flux, which alters the ion bombardment conditions and consequently affects the homogeneity of the nitrided layer [46]. In condition 2P10, the color change was observed across the entire surface rather than being confined to the edges. Nevertheless, the edges became darker than the central region of the sample, indicating greater susceptibility of the regions near the sample edges to corrosion reactions.

Fe (2p), Cr (2p), and O (1s) spectra for the nitrided and untreated conditions are presented in Figure 11. For the nitrided samples, the graphs on the left show measurements taken at the center, whereas the graphs on the right show measurements taken at the edge.

XPS spectral analysis revealed that the darkened regions on the surfaces of the nitrided samples are composed predominantly of iron oxides (FeO and Fe_2O_3). This identification was confirmed by the presence of characteristic peaks at 709 eV (FeO) and 710 eV (Fe_2O_3), which were more evident in analyses of the sample edge regions. A difference in the distribution of these oxides between distinct regions of the samples was also noted. For

conditions 2C and 2P50, the analysis of the center region (light area) did not indicate the presence of iron oxides. In contrast, measurements at the edges (dark area) revealed the presence of such compounds. For condition 2P10, the intensity of signals related to iron oxides was higher even in the central region.

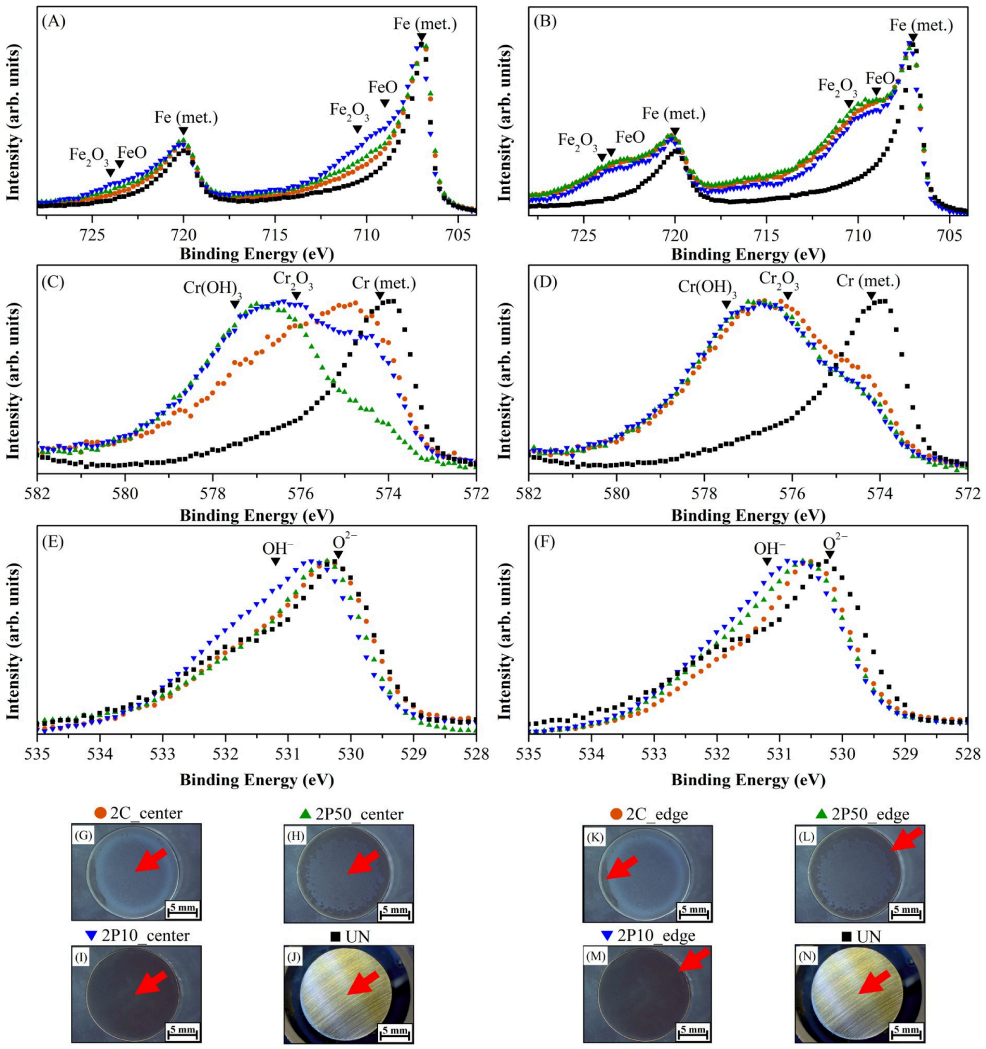


Figure 11. X-ray photoelectron spectroscopy (XPS) spectra of (**A**,**B**) Fe 2p, (**C**,**D**) Cr 2p, and (**E**,**F**) O 1s obtained for the nitrided samples (2C, 2P50, and 2P10) and the untreated sample (UN) after the potentiodynamic polarization test. The spectra on the left (**A**,**C**,**E**) correspond to measurements taken at the center of the samples, whereas those on the right (**B**,**D**,**F**) correspond to the edge regions. (**G–N**) Surface optical images of the samples after the polarization test, where red arrows indicate the analyzed regions: center (**G–J**) and edge (**K–N**) for 2C (**G**,**K**), 2P50 (**H**,**L**), 2P10 (**I**,**M**), and UN (**J**,**N**).

The formation of an iron oxide layer on the surface is associated with dissolution of the passive chromium oxide film as the potential increases during the polarization test. It occurs because, as the potential increases, the stability of iron surpasses that of chromium, favoring the precipitation of iron oxides [47]. Thus, the chromium oxide layer on sample 2P10 proved less protective, thereby allowing dissolution and subsequent formation of iron oxides. In contrast, in samples 2C and 2P50, this phenomenon was restricted to the edges. The edge effect in corrosion tests is well known due to differences in properties relative to the central region. However, in this case, the edge effect caused by the nitriding process prevailed, resulting in a region where layer uniformity was compromised by charge flux distortions and altered ion bombardment dynamics [46].

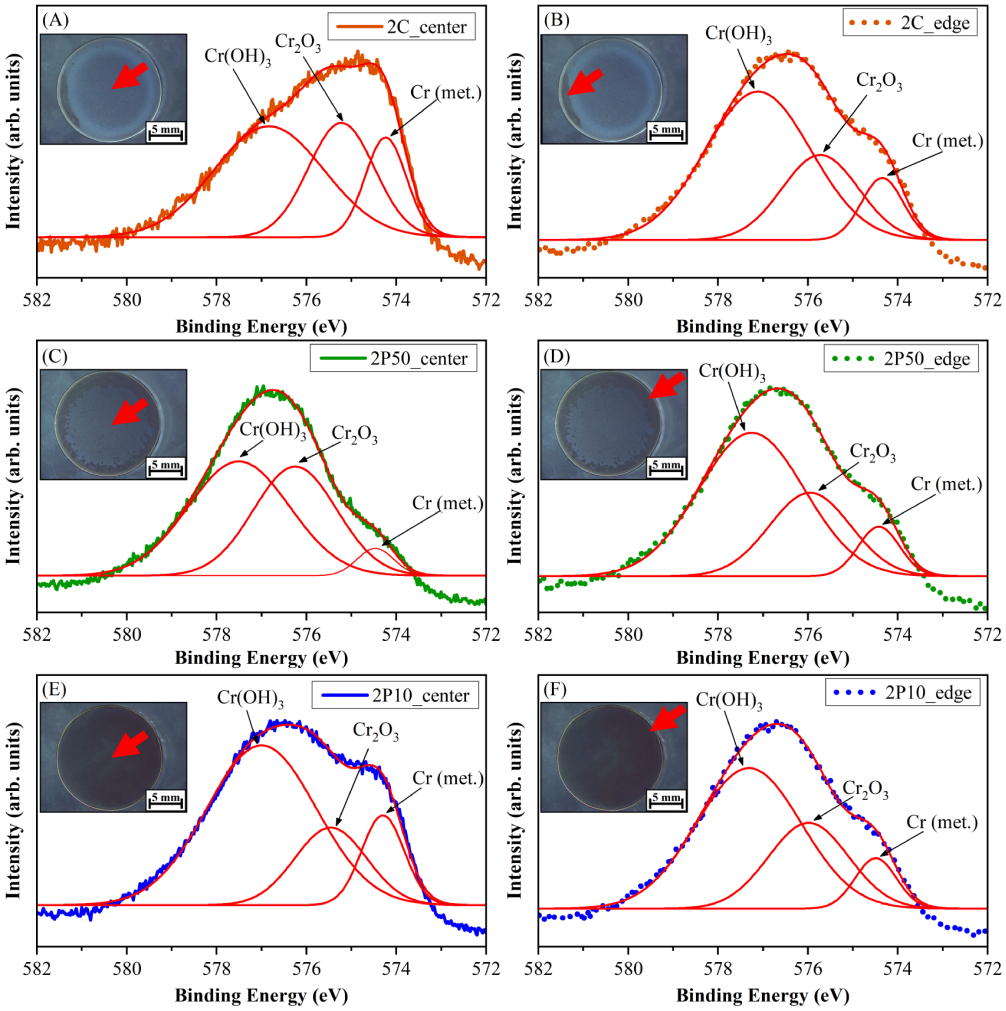


Figure 12. X-ray photoelectron spectroscopy spectra of Cr (2p) and deconvolution curves for the peaks of chromium (metallic), chromium hydroxide ($Cr(OH)_3$), and chromium oxide (Cr_2O_3), after the potentiodynamic polarization test, obtained at the edge (dashed lines) and center (solid lines) of samples (**A**,**B**) 2C, (**C**,**D**) 2P50, and (**E**,**F**) 2P10.

It was observed that condition UN did not exhibit darkened regions or peaks indicative of iron oxides in the spectra. This behavior can be attributed to the solution's pH, as the formation of iron oxides is favored at higher pH [47,48]. Accordingly, the interface between the UN sample surface and the electrolyte may have become acidified due to increased H^+ concentration, thereby inhibiting the formation of iron oxides and favoring localized corrosion.

The Cr (2p) spectra obtained in the central regions of the nitrided samples exhibited broad, poorly defined peaks, due to the overlapping of signals from metallic chromium, chromium oxide (Cr_2O_3), and chromium hydroxide ($Cr(OH)_3$). To identify the relative proportion of these compounds, peak deconvolution was performed, as presented in Figure 12A–F for the central and edge regions of the nitrided samples.

The corrosion resistance of stainless steel is closely associated with the composition and properties of its passive film, particularly the presence of chromium-rich oxides that contribute to its protective properties [49]. In the peak deconvolution of the central region, it is observed that conditions 2C and 2P50 present similar proportions of Cr_2O_3 and $Cr(OH)_3$. In contrast, condition 2P10 shows a higher proportion of $Cr(OH)_3$, leading to a less stable passive film that is more susceptible to dissolution.

When examining the deconvolution of the signals from the edge regions of the samples (dashed lines), a higher intensity of the characteristic chromium hydroxide peak is observed. The spectra indicate a similar surface composition in the darkened regions, regardless of the nitriding conditions. This behavior suggests that in this region, an alteration in ion bombardment promotes sputtering and hinders nitrogen incorporation at the surface.

These findings highlight the importance of nitrogen in corrosion resistance and underscore the significance of nitrogen concentration and process control in determining the effectiveness of the surface protection mechanisms.

4. Conclusions

Intermittent nitrogen-flow plasma nitriding effectively tailored the characteristics of the nitrided layer by controlling nitrogen incorporation, reducing nitride precipitation and brittleness with only a slight decrease in layer thickness and hardness compared with continuous-flow nitriding. In particular, the 50% nitrogen duty cycle provided an effective balance between increased hardness and the maintenance of corrosion resistance.

The electrochemical results from OCP, EIS, and potentiodynamic polarization consistently showed that corrosion resistance was strongly influenced by the nitrogen duty cycle. Continuous nitrogen flow provided the highest electrochemical stability, while a 50% duty cycle preserved corrosion resistance and passive film stability at levels comparable to those achieved under continuous nitriding. In contrast, reducing the duty cycle to 10% resulted in a pronounced deterioration of the protective behavior of the nitrided layer.

XPS analyses revealed that the superior electrochemical performance of conditions 2C and 2P50 was associated with a higher relative proportion of Cr_2O_3 and a more stable passive film. In contrast, condition 2P10 exhibited a higher proportion of $Cr(OH)_3$ and more extensive degradation of the passive film.

Despite its superior electrochemical performance, condition 2C exhibited greater susceptibility to cracking, which may compromise corrosion resistance under service conditions involving mechanical loading, as crack opening can promote electrolyte ingress and facilitate localized corrosion.

Overall, these findings demonstrate that nitrogen duty-cycle control is an effective process parameter for balancing hardness, cracking susceptibility, and corrosion resistance during plasma nitriding, highlighting the potential of intermittent nitrogen flow for advanced surface engineering applications.

Nevertheless, some practical limitations should be considered. During the periods without nitrogen flow, sputtering may contribute to nitrogen removal from the treated surface and potentially promote partial denitriding of the nitrided layer. Furthermore, the interruption and subsequent resumption of nitrogen flow require adequate control of process temperature and pressure to maintain stable, reproducible treatment conditions. Therefore, the practical application of intermittent nitrogen flow requires precise control of the process parameters, particularly during the transitions between nitrogen flow and interruption periods.

Author Contributions: Conceptualization, A.M.V., E.A.B. and M.M.; methodology, A.M.V., O.P.C. and M.M.; formal analysis, A.M.V., O.P.C., Y.E.N.d.l.R., C.E.B.M., P.C.B. and M.M.; investigation, A.M.V., O.P.C. and Y.E.N.d.l.R.; resources, P.C.B. and M.M.; data curation, A.M.V.; writing—original draft preparation, A.M.V., O.P.C., Y.E.N.d.l.R. and M.M.; writing—review and editing, A.M.V., C.E.B.M., P.C.B., E.A.B. and M.M.; visualization, A.M.V.; supervision, P.C.B., E.A.B., M.M.; funding acquisition, M.M. All authors have read and agreed to the published version of the manuscript.

Funding: This research was funded by Coordination for the Improvement of Higher Education Personnel (CAPES), Brazil (Grant No. 88887.191991/2025-00) and CNOOC/UTFPR/FUNTEF through the research project BRA-2024-RD-OC-0016-2EC.

Institutional Review Board Statement: Not applicable.

Informed Consent Statement: Not applicable.

Data Availability Statement: The data used in this research are available in the article.

Acknowledgments: The authors would like to thank Villares Metals for donating the material employed in the research and the Multi-User Center for Materials Characterization–CMCM of UTFPR-CT.

Conflicts of Interest: The authors declare no conflicts of interest.

References

1. de Araújo, E.; Bandeira, R.M.; Manfrinato, M.D.; Moreto, J.A.; Borges, R.; Vales, S.d.S.; Suzuki, P.A.; Rossino, L.S. Effect of Ionic Plasma Nitriding Process on the Corrosion and Micro-Abrasive Wear Behavior of AISI 316L Austenitic and AISI 470 Super-Ferritic Stainless Steels. *J. Mater. Res. Technol.* **2019**, *8*, 2180–2191. [CrossRef]
2. Kurelo, B.C.E.S.; De Souza, G.B.; Da Silva, S.L.R.; Lepienski, C.M.; Alves Júnior, C.; Chuproski, R.F.; Pintaúde, G. Tribo-Mechanical Behavior of Films and Modified Layers Produced by Cathodic Cage and Glow Discharge Plasma Nitriding Techniques. *Metals* **2023**, *13*, 430. [CrossRef]
3. Reinders, P.M.; Bräuer, G. A Model to Predict the S-Phase Thickness and the Change in Corrosion Behavior toward H_2SO_4 of 316L Austenitic Stainless Steel after Plasma Nitriding. *Surf. Coat. Technol.* **2023**, *475*, 130135. [CrossRef]
4. Duan, F.; Zhang, Y.; Xiong, J.; Zhou, P.; Feng, H.; Li, H.; Zhang, T.; Wang, F. Improving Corrosion Resistance of 316 L Stainless Steel by High-Pressure Electrolyte Electrochemical Nitriding. *Surf. Interfaces* **2026**, *87*, 109027. [CrossRef]
5. Tao, X.; Li, X.; Dong, H.; Matthews, A.; Leyland, A. Evaluation of the Sliding Wear and Corrosion Performance of Triode-Plasma Nitrided Fe-17Cr-20Mn-0.5N High-Manganese and Fe-19Cr-35Ni-1.2Si High-Nickel Austenitic Stainless Steels. *Surf. Coat. Technol.* **2021**, *409*, 126890. [CrossRef]
6. Xue, Y.; Zhai, L.; Xu, Y.; Wu, W.; Jiang, Y.; Gong, J. Low-Temperature Nitrocarburized 316L Stainless Steel: Residual Stress and Mechanical Properties. *Surf. Interfaces* **2025**, *62*, 106247. [CrossRef]
7. Berton, E.M.; das Neves, J.C.K.; Mafra, M.; Borges, P.C. Quenching and Tempering Effect on the Corrosion Resistance of Nitrogen Martensitic Layer Produced by SHTPN on AISI 409 Steel. *Surf. Coat. Technol.* **2020**, *395*, 125921. [CrossRef]
8. Huang, Z.; Guo, Z.-X.; Liu, L.; Guo, Y.-Y.; Chen, J.; Zhang, Z.; Li, J.-L.; Li, Y.; Zhou, Y.-W.; Liang, Y.-S. Structure and Corrosion Behavior of Ultra-Thick Nitrided Layer Produced by Plasma Nitriding of Austenitic Stainless Steel. *Surf. Coat. Technol.* **2021**, *405*, 126689. [CrossRef]
9. Lu, Y.; Li, D.; Ma, H.; Liu, X.; Wu, M.; Hu, J. Enhanced Plasma Nitriding Efficiency and Properties by Severe Plastic Deformation Pretreatment for 316L Austenitic Stainless Steel. *J. Mater. Res. Technol.* **2021**, *15*, 1742–1746. [CrossRef]
10. Yazıcı, M.; Çomaklı, O.; Yetim, T.; Yetim, A.F.; Çelik, A. Investigation of Mechanical, Tribological and Magnetic Properties after Plasma Nitriding of AISI 316L Stainless Steel Produced with Different Orientations Angles by Selective Laser Melting. *Surf. Coat. Technol.* **2023**, *467*, 129676. [CrossRef]
11. Berton, E.M.; Das Neves, J.C.K.; Mafra, M.; Borges, P.C. Nitrogen Enrichment of AISI 409 Stainless Steel by Solution Heat Treatment after Plasma Nitriding. *Kov. Mater.* **2017**, *55*, 317–321. [CrossRef]
12. Uzun, Y. Tribocorrosion Properties of Plasma Nitrided, Ti-DLC Coated and Duplex Surface Treated AISI 316L Stainless Steel. *Surf. Coat. Technol.* **2022**, *441*, 128587. [CrossRef]
13. Borgioli, F.; Galvanetto, E.; Bacci, T. Low Temperature Nitriding of AISI 300 and 200 Series Austenitic Stainless Steels. *Vacuum* **2016**, *127*, 51–60. [CrossRef]
14. Borgioli, F.; Galvanetto, E.; Bacci, T. Corrosion Behaviour of Low Temperature Nitrided Nickel-Free, AISI 200 and AISI 300 Series Austenitic Stainless Steels in NaCl Solution. *Corros. Sci.* **2018**, *136*, 352–365. [CrossRef]
15. Saravanan, P.; Raja, V.S.; Mukherjee, S. Effect of Alloyed Molybdenum on Corrosion Behavior of Plasma Immersion Nitrogen Ion Implanted Austenitic Stainless Steel. *Corros. Sci.* **2013**, *74*, 106–115. [CrossRef]
16. Baranowska, J.; Arnold, B. Corrosion Resistance of Nitrided Layers on Austenitic Steel. *Surf. Coat. Technol.* **2006**, *200*, 6623–6628. [CrossRef]
17. Fossati, A.; Borgioli, F.; Galvanetto, E.; Bacci, T. Glow-Discharge Nitriding of AISI 316L Austenitic Stainless Steel: Influence of Treatment Time. *Surf. Coat. Technol.* **2006**, *200*, 3511–3517. [CrossRef]
18. Fossati, A.; Borgioli, F.; Galvanetto, E.; Bacci, T. Corrosion Resistance Properties of Glow-Discharge Nitrided AISI 316L Austenitic Stainless Steel in NaCl Solutions. *Corros. Sci.* **2006**, *48*, 1513–1527. [CrossRef]
19. Li, G.; Peng, Q.; Li, C.; Wang, Y.; Gao, J.; Chen, S.; Wang, J.; Shen, B. Effect of DC Plasma Nitriding Temperature on Microstructure and Dry-Sliding Wear Properties of 316L Stainless Steel. *Surf. Coat. Technol.* **2008**, *202*, 2749–2754. [CrossRef]

20. Yazıcı, M.; Çomaklı, O.; Yetim, T.; Yetim, A.F.; Çelik, A. The Effect of Plasma Nitriding Temperature on the Electrochemical and Semiconducting Properties of Thin Passive Films Formed on 316 L Stainless Steel Implant Material in SBF Solution. *Surf. Coat. Technol.* **2015**, *261*, 181–188. [CrossRef]
21. Manova, D.; Günther, C.; Bergmann, A.; Mändl, S.; Neumann, H.; Rauschenbach, B. Influence of Temperature on Layer Growth as Measured by in Situ XRD Observation of Nitriding of Austenitic Stainless Steel. *Nucl. Instrum. Methods Phys. Res. Sect. B Beam Interact. Mater. At.* **2013**, *307*, 310–314. [CrossRef]
22. Borgioli, F.; Fossati, A.; Galvanetto, E.; Bacci, T. Glow-Discharge Nitriding of AISI 316L Austenitic Stainless Steel: Influence of Treatment Temperature. *Surf. Coat. Technol.* **2005**, *200*, 2474–2480. [CrossRef]
23. De Las Heras, E.; Ybarra, G.; Lamas, D.; Cabo, A.; Dalibon, E.L.; Brühl, S.P. Plasma Nitriding of 316L Stainless Steel in Two Different N2-H2 Atmospheres—Influence on Microstructure and Corrosion Resistance. *Surf. Coat. Technol.* **2017**, *313*, 47–54. [CrossRef]
24. Fernandes, F.A.P.; Christiansen, T.L.; Winther, G.; Somers, M.A.J. Measurement and Tailoring of Residual Stress in Expanded Austenite on Austenitic Stainless Steel. *Mater. Sci. Eng. A* **2017**, *701*, 167–173. [CrossRef]
25. Vianna, A.M.; Brunetti, C.; Mafra, M.; dos Reis, R.F.; Villanova, R.L.; Bernardelli, E.A. Plasma Nitriding of ISO 5832-1 Stainless Steel at 425 °C with Intermittent Nitrogen Flow. *Mater. Res.* **2020**, *23*, e20200249. [CrossRef]
26. dos Reis, R.F.; Mori da Silva, P.G.H.; Villanova, R.L.; Vianna, A.M.; Bernardelli, E.A. Plasma Nitriding of ISO 5832-1 Stainless Steel with Intermittent Nitrogen Flow at 450 °C. *Mater. Res.* **2020**, *23*, e20190501. [CrossRef]
27. Sphair, A.C.; Vianna, A.M.; Lepienski, C.M.; de Souza, G.B.; Bernardelli, E.A.; Mafra, M. Influence of Plasma Nitriding Under Pulsed Nitrogen Flow on Expanded Austenite Formation and Surface Performance of ISO 5832-1 Stainless Steel. *Coatings* **2025**, *15*, 975. [CrossRef]
28. Cullity, B.D.; Stock, S.R. *Elements of X-Ray Diffraction*; Pearson: Harlow, UK, 2014; ISBN 1-269-37450-8.
29. Öztürk, O.; Williamson, D.L. Phase and Composition Depth Distribution Analyses of Low Energy, High Flux N Implanted Stainless Steel. *J. Appl. Phys.* **1995**, *77*, 3839–3850. [CrossRef]
30. Orazem, M.E.; Tribollet, B. *Electrochemical Impedance Spectroscopy*, 1st ed.; Wiley: Hoboken, NJ, USA, 2008; ISBN 978-0-470-04140-6.
31. Bottoli, F.; Winther, G.; Christiansen, T.L.; Dahl, K.V.; Somers, M.A.J. Low-Temperature Nitriding of Deformed Austenitic Stainless Steels with Various Nitrogen Contents Obtained by Prior High-Temperature Solution Nitriding. *Metall. Mater. Trans. A* **2016**, *47*, 4146–4159. [CrossRef]
32. Czerwiec, T.; He, H.; Weber, S.; Dong, C.; Michel, H. On the Occurrence of Dual Diffusion Layers during Plasma-Assisted Nitriding of Austenitic Stainless Steel. *Surf. Coat. Technol.* **2006**, *200*, 5289–5295. [CrossRef]
33. Manova, D.; Mändl, S. Initial Phase Formation during Nitriding of Austenitic Stainless Steel. *Surf. Coat. Technol.* **2023**, *456*, 129258. [CrossRef]
34. Borgioli, F. The Corrosion Behavior in Different Environments of Austenitic Stainless Steels Subjected to Thermochemical Surface Treatments at Low Temperatures: An Overview. *Metals* **2023**, *13*, 776. [CrossRef]
35. Teng, Y.; Guo, Y.-Y.; Zhang, M.; Yang, Y.-J.; Huang, Z.; Zhou, Y.-W.; Wu, F.-Y.; Liang, Y.-S. Effect of Cr/CrNx Transition Layer on Mechanical Properties of CrN Coatings Deposited on Plasma Nitrided Austenitic Stainless Steel. *Surf. Coat. Technol.* **2019**, *367*, 100–107. [CrossRef]
36. Jespersen, F.N.; Hattel, J.H.; Somers, M.A.J. Modelling the Evolution of Composition-and Stress-Depth Profiles in Austenitic Stainless Steels during Low-Temperature Nitriding. *Model. Simul. Mater. Sci. Eng.* **2016**, *24*, 025003. [CrossRef]
37. Han, Z.; Lu, J.; Yin, C.; Lai, P.; Zhuang, W.; Li, L.; Wang, J.; Zhang, L.; Guo, X. Composition, Microstructure, and Phase Evolution of 17-4PH Stainless Steel with a Work-Hardened Layer in the Low-Temperature Plasma Nitriding Process. *Surf. Coat. Technol.* **2022**, *451*, 128950. [CrossRef]
38. Shen, H.; Wang, L. Mechanism and Properties of Plasma Nitriding AISI 420 Stainless Steel at Low Temperature and Anodic (Ground) Potential. *Surf. Coat. Technol.* **2020**, *403*, 126390. [CrossRef]
39. Moskalioviene, T.; Galdikas, A. Kinetic Model of Anisotropic Stress Assisted Diffusion of Nitrogen in Nitrided Austenitic Stainless Steel. *Surf. Coat. Technol.* **2019**, *366*, 277–285. [CrossRef]
40. Christiansen, T.; Dahl, K.V.; Somers, M.A.J. Nitrogen Diffusion and Nitrogen Depth Profiles in Expanded Austenite: Experimental Assessment, Numerical Simulation and Role of Stress. *Mater. Sci. Technol.* **2008**, *24*, 159–167. [CrossRef]
41. Borgioli, F.; Galvanetto, E.; Bacci, T. Surface Modification of a Nickel-Free Austenitic Stainless Steel by Low-Temperature Nitriding. *Metals* **2021**, *11*, 1845. [CrossRef]
42. Kalisz, M.; Grobelny, M.; Świniarski, M.; Mazur, M.; Wojcieszak, D.; Zdrojek, M.; Judek, J.; Domaradzki, J.; Kaczmarek, D. Comparison of Structural, Mechanical and Corrosion Properties of Thin TiO_2/Graphene Hybrid Systems Formed on Ti–Al–V Alloys in Biomedical Applications. *Surf. Coat. Technol.* **2016**, *290*, 124–134. [CrossRef]
43. Luiz, L.A.; Kurelo, B.C.E.S.; de Souza, G.B.; de Andrade, J.; Marino, C.E.B. Effect of Nitrogen Plasma Immersion Ion Implantation on the Corrosion Protection Mechanisms of Different Stainless Steels. *Mater. Today Commun.* **2021**, *28*, 102655. [CrossRef]

44. Revilla, R.I.; Wouters, B.; Andreatta, F.; Lanzutti, A.; Fedrizzi, L.; De Graeve, I. EIS Comparative Study and Critical Equivalent Electrical Circuit (EEC) Analysis of the Native Oxide Layer of Additive Manufactured and Wrought 316L Stainless Steel. *Corros. Sci.* **2020**, *167*, 108480. [CrossRef]
45. Nuñez de la Rosa, Y.; Palma Calabokis, O.; Ballesteros-Ballesteros, V.; Tafur, C.L.; Borges, P.C. Assessment of the Pitting, Crevice Corrosion, and Mechanical Properties of Low-Temperature Plasma-Nitrided Inconel Alloy 718. *Metals* **2023**, *13*, 1172. [CrossRef]
46. Alves, C.; de Araújo, F.O.; Ribeiro, K.J.B.; da Costa, J.A.P.; Sousa, R.R.M.; de Sousa, R.S. Use of Cathodic Cage in Plasma Nitriding. *Surf. Coat. Technol.* **2006**, *201*, 2450–2454. [CrossRef]
47. Olsson, C.-O.A.; Landolt, D. Passive Films on Stainless Steels—Chemistry, Structure and Growth. *Electrochim. Acta* **2003**, *48*, 1093–1104. [CrossRef]
48. Lynch, B.; Wiame, F.; Maurice, V.; Marcus, P. XPS Study of Oxide Nucleation and Growth Mechanisms on a Model FeCrNiMo Stainless Steel Surface. *Appl. Surf. Sci.* **2022**, *575*, 151681. [CrossRef]
49. Ning, K.; Zhang, Y.; Xue, Q. Atomic Scale Insights into Chloride Induced Degradation of Stainless Steel Passive Films. *Surf. Interfaces* **2026**, *95*, 109869. [CrossRef]

Disclaimer/Publisher's Note: The statements, opinions and data contained in all publications are solely those of the individual author(s) and contributor(s) and not of MDPI and/or the editor(s). MDPI and/or the editor(s) disclaim responsibility for any injury to people or property resulting from any ideas, methods, instructions or products referred to in the content.